Dynamics of large-scale quantities in Rayleigh-Bénard convection

Ambrish Pandey,[*] Abhishek Kumar,[†] Anando G. Chatterjee,[‡] and Mahendra K. Verma[§]

Department of Physics, Indian Institute of Technology, Kanpur 208016, India

(Received 24 January 2016; revised manuscript received 14 September 2016; published 7 November 2016)

In this paper we estimate the relative strengths of various terms of the Rayleigh-Bénard equations. Based on these estimates and scaling analysis, we derive a general formula for the large-scale velocity U or the Péclet number that is applicable for arbitrary Rayleigh number Ra and Prandtl number Pr. Our formula fits reasonably well with the earlier simulation and experimental results. Our analysis also shows that the wall-bounded convection has enhanced viscous force compared to free turbulence. We also demonstrate how correlations deviate the Nusselt number scaling from the theoretical prediction of $Ra^{1/2}$ to the experimentally observed scaling of nearly $Ra^{0.3}$.

I. INTRODUCTION

Modeling the large-scale quantities in a turbulent flow is very important in many applications, e.g., fluid and magnetohydrodynamic turbulence, Rayleigh-Bénard convection (RBC), rotating turbulence, etc. [1–5]. One such quantity is the magnitude of the large-scale velocity that plays a critical role in physical processes. In this paper we will quantify this and other related quantities for RBC.

RBC is an idealized version of thermal convection in which a thin layer of fluid confined between two horizontal plates separated by a distance d is heated from below and cooled from the top. The properties of RBC are specified using two nondimensional parameters: the Rayleigh number (Ra), which is the ratio of the buoyancy term and the diffusion term, and the Prandtl number (Pr), which is the ratio of kinematic viscosity ν and thermal diffusivity κ [6–9]. Some of the important quantities of interest in RBC are the large-scale velocity U or the Péclet number (Pe) $Pe = Ud/\kappa$ and the Nusselt number (Nu), which is the ratio of the total heat flux to the conductive heat flux. Note that the Reynolds number (Re) is $Re = Pe/Pr$.

The Péclet and Nusselt numbers are strong functions of Pr as shown by Grossmann and Lohse [referred to as (GL)] [10–13]. According to GL scaling, for small and moderate Pr's, $Pe \sim \sqrt{Ra\,Pr}$, but for large Pr's, $Pe \sim Ra^{3/5}$. The above scalings have been verified in many experiments [14–21] and numerical simulations [22–30]. In this paper we derive a general formula for the Pe, of which the aforementioned relations are limiting cases, by comparing the relative strengths of the nonlinear, pressure, buoyancy, and viscous terms and quantifying them using the numerical data. Our derivation of the Pe formula differs from the formalism of Grossmann and Lohse [10–13]; comparison between the two approaches will be discussed towards the end of the paper.

Before describing the Péclet number formula, we briefly discuss the properties of the temperature fluctuations. We normalize the temperature by the temperature difference between the plates Δ and the vertical coordinate z by the

———————
[*]ambrishiitk@gmail.com
[†]abhkr@iitk.ac.in
[‡]anandogc@iitk.ac.in
[§]mkv@iitk.ac.in

plate distance d. The profile of the plane-averaged temperature $T_m(z)$ shown in Fig. 1 exhibits an approximate constant value of $1/2$ in the bulk and steep variations in the thermal boundary layer. It is customary to write RBC equations in terms of the temperature fluctuation from the conduction state $\theta(x,y,z)$, where $T = T_c(z) + \theta(x,y,z)$ with $T_c = 1 - z$ as the temperature profile for the conduction state. The planar mean of θ, $\theta_m(z)$ is illustrated in Fig. 1.

The momentum equation for RBC is

$$\partial_t \mathbf{u} + \mathbf{u} \cdot \nabla \mathbf{u} = -\nabla \sigma + \alpha g \theta \hat{z} + \nu \nabla^2 \mathbf{u}, \qquad (1)$$

where $\mathbf{u}$ and σ are the velocity and pressure fields, respectively, α is the thermal expansion coefficient, and g is the acceleration due to gravity. Here we have taken the density to be unity. Under a steady state ($\langle \partial_t \mathbf{u} \rangle = 0$), the acceleration of a fluid parcel $\mathbf{u} \cdot \nabla \mathbf{u}$ is provided by the pressure gradient $-\nabla \sigma$, buoyancy $\alpha g \theta \hat{z}$, and the viscous term $\nu \nabla^2 \mathbf{u}$. For a viscous flow, the net force or acceleration is very small, and the viscous force balances the buoyancy. However, in the turbulent regime, the pressure gradient dominates the buoyancy and viscous forces (see Fig. 2). We quantify these accelerations using numerical data that help us understand the scaling of the Péclet number and related quantities for arbitrary Pr's and Ra's. The velocity Fourier modes $\hat{\mathbf{u}}(0,0,k_z) = 0$ are due to incompressibility and no-mean flow condition. Hence $\hat{\sigma}_m(0,0,k_z)$ corresponding to $\theta_m(z)$ follows a relation: $ik_z \hat{\sigma}_m(0,0,k_z) = \alpha g \hat{\theta}_m(0,0,k_z)$ or $d\sigma_m(z)/dz = \alpha g \theta_m$. Therefore, in the momentum equation, the Fourier modes other than $(0,0,k_z)$ involve $\theta_{\text{res}} = \theta - \theta_m$ and $\sigma_{\text{res}} = \sigma - \sigma_m$, respectively (see the Appendix).

II. NUMERICAL METHOD

We solve the RBC equations [6–9] in a three-dimensional unit box for $Pr = 1, 6.8, 10^2, 10^3$ and Rayleigh numbers between 10^6 and 5×10^8 on grids of $60^3, 80^3, 100^3$, and 256^3 using the finite volume code OPENFOAM [31]. We employ the no-slip boundary condition for the velocity field at all the walls, the conducting boundary condition at the top and bottom walls, and the insulating boundary condition at the vertical walls. For time stepping we use the second-order Crank-Nicolson scheme. To resolve the boundary layers we employ a nonuniform mesh with a higher concentration of grid points (greater than 4–6) near the boundaries [32,33]. Table I includes a summary of the numerical simulations
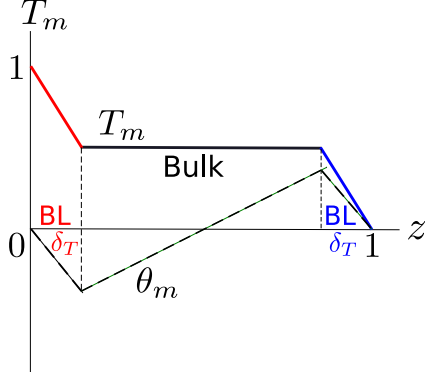
FIG. 1. The plane-averaged temperature profile $T_m(z)$ exhibits a near constant value in the bulk and steep variations in the thermal boundary layers whose thicknesses are δ_T. The normalized temperature fluctuation is $\theta = T + z - 1$; the figure also exhibits its plane-averaged profile $\theta_m(z)$.

FIG. 2. Schematic of acceleration **a** of a fluid parcel that is rising against gravity: (a) in the turbulent regime, **a** is provided primarily by the pressure gradient $-\nabla\sigma$; (b) in the viscous regime, $\mathbf{a} \approx 0$ with the buoyancy and viscous terms balancing each other. The directions of the forces are reversed for a descending fluid parcel. Note that buoyancy acts downward for the fluid parcels colder than the background.

performed. We have performed the grid-independence test for Pr = 1, Ra = 10^8 by performing simulations on 100^3 and 256^3 grids and find that the Nusselt and Péclet numbers are different by approximately 3% and 1%, respectively.

We compute $U = \sqrt{\langle u^2 \rangle}$ [root mean square (rms) value] first by volume averaging u^2 over the entire computational domain and then by performing temporal average over many snapshots (see Table I). We also estimate the strengths of various terms of the momentum equation by a similar averaging process. These values are depicted in Figs. 3(a) and 3(a) for Pr = 1 and 10^2 with Ra's ranging from 10^6 to 5×10^8. The flow is turbulent for Pr = 1 and Ra = $5 \times 10^7, 10^8, 5 \times 10^8$ whose respective Reynolds numbers are approximately 1103,

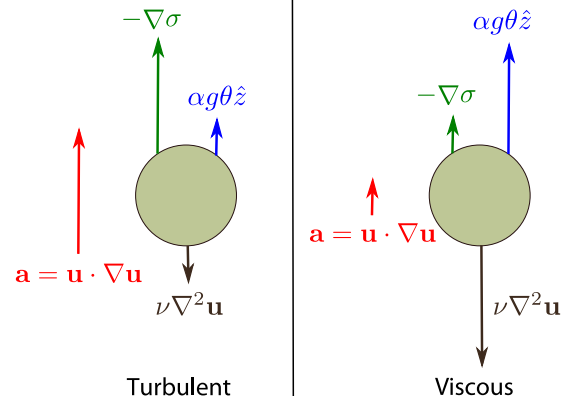1537, and 3408. But the flow is laminar for all Ra's when Pr = 10^2. Clearly, the numerical values are consistent with the schematic of Fig. 2. The acceleration in the turbulent regime is dominated by the pressure gradient with small contributions from the buoyancy and viscous terms. However, in the viscous regime, the viscous term balances the buoyancy yielding a very small acceleration. Therefore, all the terms of the momentum equation balance reasonably well. To test this out, we compute the vector sum of all the terms for a given Ra, i.e., $S = |\mathbf{u} \cdot \nabla \mathbf{u}| - |(-\nabla\sigma)_{\mathrm{res}}| - |\alpha g \theta_{\mathrm{res}} \hat{z}| + |\nu \nabla^2 \mathbf{u}|$ and the

TABLE I. Details of our numerical simulations performed in a unit box: the Pr, the Ra, grid points (N^3), the Nu, the Pe, averaged values of the nonlinear term, pressure gradient, buoyancy, viscous force, and the number of snapshots over which the time averaging has been performed. The terms of the momentum equation are normalized by $Z = \alpha g \Delta$.

| Pr	Ra	N^3	Nu	Pe	$\lvert\mathbf{u}\cdot\nabla\mathbf{u}\rvert/Z$	$\lvert(-\nabla\sigma)_{\mathrm{res}}\rvert/Z$	$\lvert\alpha g\theta\hat{z}\rvert/Z$	$\lvert\nu\nabla^2\mathbf{u}\rvert/Z$	Snapshots
1	1×10^6	60^3	8.0	146.1	0.152	0.110	0.0955	0.110	100
1	2×10^6	60^3	10.0	211.3	0.177	0.126	0.0883	0.0934	200
1	5×10^6	60^3	13.4	340.3	0.213	0.146	0.0788	0.0749	200
1	1×10^7	80^3	16.3	485.4	0.234	0.157	0.0715	0.0707	50
1	2×10^7	80^3	20.2	687.4	0.266	0.168	0.0653	0.0608	200
1	5×10^7	80^3	26.8	1103	0.318	0.187	0.0575	0.0486	178
1	1×10^8	100^3	32.9	1554	0.359	0.200	0.0526	0.0480	100
1	1×10^8	256^3	31.9	1537	0.348	0.205	0.0529	0.0789	35
1	5×10^8	256^3	51.2	3408	0.472	0.233	0.0429	0.0559	34
6.8	1×10^6	60^3	8.4	182.7	0.0273	0.0160	0.0825	0.106	200
6.8	2×10^6	60^3	9.9	252.8	0.0333	0.0221	0.0745	0.0865	200
6.8	5×10^6	60^3	13.1	413.6	0.0413	0.0272	0.0645	0.0691	250
6.8	1×10^7	80^3	16.2	608.6	0.0474	0.0310	0.0581	0.0669	163
6.8	2×10^7	80^3	20.3	903.2	0.0558	0.0352	0.0518	0.0570	200
6.8	5×10^7	80^3	27.7	1536	0.0696	0.0419	0.0452	0.0456	165
10^2	1×10^6	60^3	8.5	190.7	1.94×10^{-3}	1.02×10^{-3}	0.0792	0.108	300
10^2	2×10^6	60^3	11.2	278.2	2.19×10^{-3}	1.01×10^{-3}	0.0731	0.0938	180
10^2	5×10^6	60^3	14.5	500.0	2.91×10^{-3}	1.42×10^{-3}	0.0587	0.0732	250
10^2	1×10^7	80^3	17.1	704.2	3.69×10^{-3}	2.15×10^{-3}	0.0531	0.0659	250
10^2	2×10^7	80^3	20.7	1044	4.47×10^{-3}	2.62×10^{-3}	0.0467	0.0556	200
10^2	5×10^7	80^3	27.7	1826	6.08×10^{-3}	3.53×10^{-3}	0.0395	0.0460	250
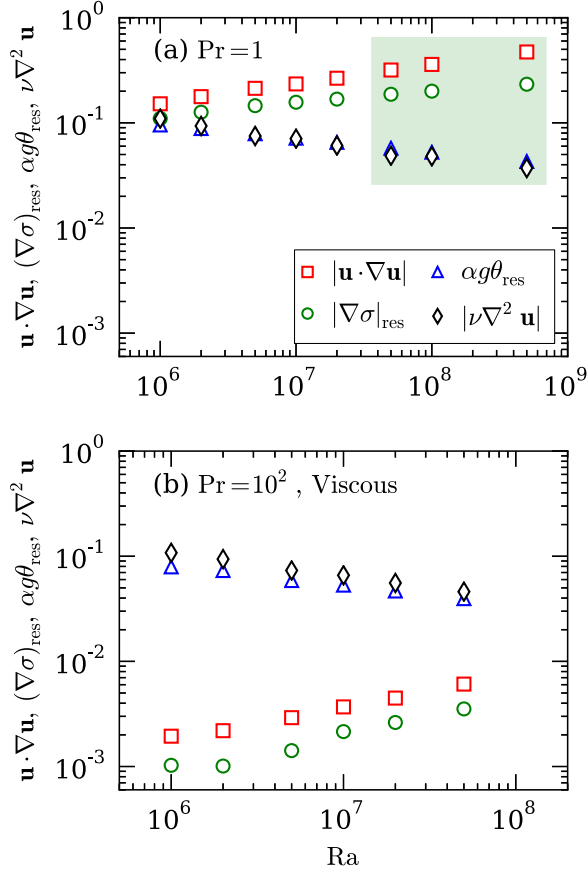
FIG. 3. Plots comparing the rms values of various terms of the momentum equation $|\mathbf{u} \cdot \nabla \mathbf{u}|$, $|(\nabla \sigma)_{\mathrm{res}}|$, $\alpha g \theta_{\mathrm{res}}$, and $|\nu \nabla^2 \mathbf{u}|$ as functions of Ra for (a) $\mathrm{Pr} = 1$ and (b) $\mathrm{Pr} = 10^2$. In the turbulent regime [the shaded region of (a)], $|\mathbf{u} \cdot \nabla \mathbf{u}| \approx |\nabla \sigma| \gg \alpha g \theta_{\mathrm{res}}, |\nu \nabla^2 \mathbf{u}|$; in the viscous regime (b), $\alpha g \theta_{\mathrm{res}}, |\nu \nabla^2 \mathbf{u}| \gg |\mathbf{u} \cdot \nabla \mathbf{u}|, |\nabla \sigma|$.

most dominant term among them, i.e., $M = \mathrm{Maximum}(|\mathbf{u} \cdot \nabla \mathbf{u}|, |(-\nabla \sigma)_{\mathrm{res}}|, |\alpha g \theta_{\mathrm{res}} \hat{z}|, |\nu \nabla^2 \mathbf{u}|)$. We observe that the ratio S/M varies from 19% to 53%. We also remark that the buoyancy in RBC is $\alpha g (T - T_{\mathrm{ref}}) \hat{z}$. The temperature T of a cold fluid parcel (moving downward) is lower than that of the reference fluid temperature T_{ref}. Therefore the force due to the density difference on a colder fluid parcel traveling downwards is in the $-\hat{z}$ direction, and hence the forces on it are opposite to that in Fig. 2. Thus, the net force balance holds for both ascending and descending fluid parcels.

III. RESULTS

To quantify the terms of the momentum equation, we perform a scaling analysis of the momentum equation that yields

$$c_1 \frac{U^2}{d} = c_2 \frac{U^2}{d} + c_3 \alpha g \Delta - c_4 \nu \frac{U}{d^2}, \qquad (2)$$

where $c_1 = |\mathbf{u} \cdot \nabla \mathbf{u}|/(U^2/d)$, $c_2 = |(\nabla \sigma)_{\mathrm{res}}|/(U^2/d)$, $c_3 = \theta_{\mathrm{res}}/\Delta$ and $c_4 = |\nabla^2 \mathbf{u}|/(U/d^2)$ are dimensionless coefficients. In this paper, we compute the coefficients c_i for $\mathrm{Pr} =$
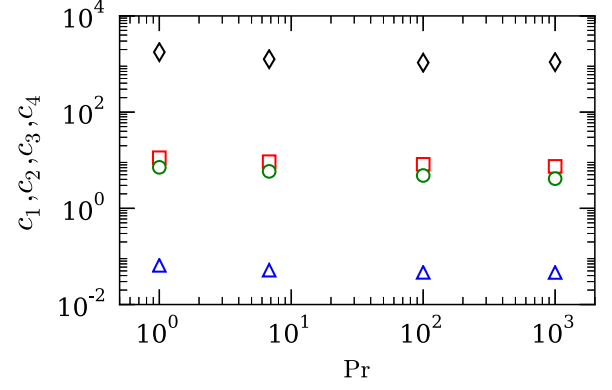

FIG. 4. Plots of c_1 (red squares), c_2 (green circles), c_3 (blue triangles), and c_4 (black diamonds) of Eqs. (3a)–(3d) as functions of the Pr for $\mathrm{Ra} = 2 \times 10^7$. All c_i's are weak functions of the Pr.

$1, 6.8, 100,$ and 1000. Our numerical computation yields

$$c_1 = 1.5 \, \mathrm{Ra}^{0.10} \mathrm{Pr}^{-0.06}, \qquad (3a)$$

$$c_2 = 1.6 \, \mathrm{Ra}^{0.09} \mathrm{Pr}^{-0.08}, \qquad (3b)$$

$$c_3 = 0.75 \, \mathrm{Ra}^{-0.15} \mathrm{Pr}^{-0.05}, \qquad (3c)$$

$$c_4 = 20 \, \mathrm{Ra}^{0.24} \mathrm{Pr}^{-0.08}. \qquad (3d)$$

The errors in the exponents are $\lesssim 0.01$, whereas the prefactors are uncertain by approximately 10%. However in the c_4 vs the Ra scaling, the exponent 0.24 is uncertain by approximately 30%. Clearly the coefficients are weak functions of the Pr (see Fig. 4), but they show significant variations with the Ra. This aspect is in contrast to *unbounded flows* (without walls) where the coefficients are independent of parameters. We attribute the above scaling to the thermal plates or *bounded flow*. Note that the Ra dependence of c_4 leads to an enhanced viscous force for RBC compared to free turbulence. In our simulations, $1 \leqslant \mathrm{Pr} \leqslant 10^2$ and $\mathrm{Ra} \leqslant 5 \times 10^8$, hence c_i's of Eqs. (3a)–(3d) may get altered for a larger Ra and an extreme Pr. Also, c_i's should depend, at least weakly, on geometry and aspect ratio. Yet we believe that our formula, to be described below, should provide an approximate description of U for large Ra's and extreme Pr's.

Multiplication of Eq. (2) with d^3/κ^2 yields the following equation for the Péclet number:

$$c_1 \mathrm{Pe}^2 = c_2 \mathrm{Pe}^2 + c_3 \mathrm{Ra}\,\mathrm{Pr} - c_4 \mathrm{Pe}\,\mathrm{Pr}, \qquad (4)$$

whose solution is

$$\mathrm{Pe} = \frac{-c_4 \mathrm{Pr} + \sqrt{c_4^2 \mathrm{Pr}^2 + 4 c_3 (c_1 - c_2) \mathrm{Ra}\,\mathrm{Pr}}}{2(c_1 - c_2)}. \qquad (5)$$

A combination of Eqs. (5), (3a)–(3d) provide us a predictive formula for the Péclet number for arbitrary Pr's and Ra's. We test our formula with numerical results of ours, Reeuwijk *et al.* [23], Silano *et al.* [24], and Scheel and Schumacher [34], and the experimental results of Niemela *et al.* [18], Xin and Xia [14], and Cioni *et al.* [15]. The predictions of Eq. (5) for $\mathrm{Pr} = 0.022$ and $\mathrm{Pr} = 6.8$ have been multiplied with 2.5 and 1.2, respectively, to fit the experimental results from Cioni *et al.* [15] and Xin and Xia [14]. As shown in Fig. 5, our formula describes the numerical and experimental data reasonably well
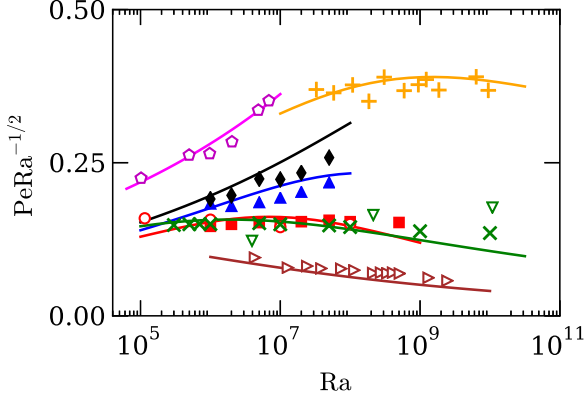
FIG. 5. Plot of the normalized Péclet number $\mathrm{Pe}\,\mathrm{Ra}^{-1/2}$ as a function of the Ra for different Pr's. Our formula for the Pe [Eq. (5)] (shown as the continuous curves) fits reasonably well with the numerical results of ours (Pr = 1, red squares; Pr = 6.8, blue triangles; Pr = 10^2, black diamonds), Scheel and Schumacher [34] (Pr = 0.7, green crosses), Reeuwijk *et al.* [23] (Pr = 1, red circles), and Silano *et al.* [24] (Pr = 10^3, magenta pentagons), and the experimental results of Cioni *et al.* [15] (Pr ≈ 0.022, brown right-triangles) and Xin and Xia [14] (Pr ≈ 6.8, orange pluses). The agreement is deficient for the experimental result of Niemela *et al.* [18] (Pr ≈ 0.7, green down-triangles), possibly due to various factors discussed in the text.

for Prandtl numbers ranging from 0.025 to 1000 and for various geometries. However the above factors (2.5 and 1.2) and the discrepancy between our predictions and the results of Niemela *et al.* [18] are due to the aforementioned uncertainty in c_i's, geometrical factors, aspect ratio dependence, and different definitions used for U.

The limiting cases of the Pe formula of Eq. (5) along with Eqs. (3a)–(3d) yield *turbulent* and *viscous* regimes. For $c_4^2\mathrm{Pr}^2 \ll 4c_3(c_1 - c_2)\mathrm{Ra}\,\mathrm{Pr}$ or $\mathrm{Ra} \gg 10^6\mathrm{Pr}$, we obtain the turbulent regime with

$$\mathrm{Pe} = \sqrt{\frac{c_3}{|c_1 - c_2|}\mathrm{Ra}\,\mathrm{Pr}} \approx \sqrt{7.5\,\mathrm{Pr}}\,\mathrm{Ra}^{0.38}. \qquad (6)$$

For mercury (Pr = 0.025), the above formula yields $(\mathrm{Pe})_{\mathrm{theory}} = 0.38\,\mathrm{Ra}^{0.38}$, which is in reasonable agreement with the finding of Cioni *et al.* [15] that $(\mathrm{Pe})_{\mathrm{expt}} = 0.24\,\mathrm{Ra}^{0.43}$ in their convection experiment with mercury. However, for Pr ≈ 1 and large Ra's, many authors [13,14,16,18,22,23,26,27,34] as well our numerical simulation show that $\mathrm{Pe} \sim \mathrm{Ra}^{0.51}$ not $\mathrm{Pe} \sim \mathrm{Ra}^{0.38}$. This is because the condition $\mathrm{Ra} \gg 10^6\mathrm{Pr}$ is not satisfied in these systems (except for Refs. [18] and [34]). We remark that Eqs. (3a)–(3d) and the condition $\mathrm{Ra} \gg 10^6\mathrm{Pr}$ are derived from our numerical simulations for moderate values of the Ra and the Pr; these equations may change somewhat for larger Rayleigh and Prandtl numbers. Aspect ratio and geometry could also affect the scaling of c_i's. Yet, our Pe formula describes the earlier experimental and numerical simulations reasonably well (see Fig. 5).

The other limiting case (viscous regime) $c_4^2\mathrm{Pr}^2 \gg 4c_3(c_1 - c_2)\mathrm{Ra}\,\mathrm{Pr}$ yields $\mathrm{Pe} = (c_3/c_4)\mathrm{Ra} \approx 0.0375\,\mathrm{Ra}^{0.61}$, which is independent of the Pr as observed in several numerical simulations and experiments [13,19,24,29,30]. An application of the above to the Earth's mantle [35–37] with param-

TABLE II. The Ra dependence of the normalized correlation function $C_{u\theta_{\mathrm{res}}} = \langle u_z\theta_{\mathrm{res}}\rangle/[\langle u_z^2\rangle^{1/2}\langle\theta_{\mathrm{res}}^2\rangle^{1/2}]$, $\langle\theta_{\mathrm{res}}^2\rangle^{1/2}$, $\langle u_z^2\rangle^{1/2}$, Nu, and ϵ_u computed using numerical data. The data in the shaded region of Fig. 3(a) for Pr = 1 belong to the turbulent regime whereas that of Pr = 10^2 belong to the viscous regime. The functional forms in the table are based on our numerical simulations. The errors in the exponents are around 5%–10% for all quantities.

	Turbulent regime	Viscous regime
$C_{u\theta_{\mathrm{res}}}$	$\mathrm{Ra}^{-0.05}$	$\mathrm{Ra}^{-0.07}$
$\langle\theta_{\mathrm{res}}^2\rangle^{1/2}$	$\mathrm{Ra}^{-0.13}$	$\mathrm{Ra}^{-0.18}$
$\langle u_z^2\rangle^{1/2}$	$\mathrm{Ra}^{0.51}$	$\mathrm{Ra}^{0.58}$
Nu	$\mathrm{Ra}^{0.32}$	$\mathrm{Ra}^{0.33}$
ϵ_u	$(U^3/d)\mathrm{Ra}^{-0.21}$	$(\nu U^2/d^2)\mathrm{Ra}^{0.17}$

eters of $d \approx 2900$ km, $\kappa \approx 10^{-6}$ m²/s, Ra $\approx 5 \times 10^7$, Pr $\approx 10^{23}$–10^{24}, and $U \approx 20$ mm/yr yields $(\mathrm{Pe})_{\mathrm{obs}} \approx 1840$, which is close to our prediction that $(\mathrm{Pe})_{\mathrm{theory}} \approx 1580$.

The effects of the thermal plates and the boundary layers come into play in several different ways in our analysis. First, the thermal boundary layers at the two walls induce a mean temperature profile $\theta_m(z)$ (see Fig. 1), and only $\theta_{\mathrm{res}} = \theta - \theta_m(z)$ participates in the momentum equation. Second, the boundary layers induce the Ra dependence on c_i's [see Eqs. (3a)–(3d)]. Note that in unbounded flows (without walls) the corresponding c_i's are expected to be constants, i.e., independent of system parameters, such as the Ra. Also, the ratio of the nonlinear term and the viscous term of Eq. (2) is $(Ud/\nu)(c_1/c_4) \sim \mathrm{Re}\,\mathrm{Ra}^{-0.14}$, not just the Re as in unbounded flows. Thus, the thermal plates or the boundary layers enhance the dissipation in the RBC flows compared to the unbounded flows. We show below that a similar behavior is observed for the Nusselt number and the viscous dissipation rates.

The anisotropy induced by the thermal plates has important consequences on the heat transport and dissipation rates: $\langle u_z\theta\rangle \neq 0$, unlike $\langle u_z\theta\rangle = 0$ for any isotropic flow. The Nusselt number $\mathrm{Nu} \sim C_{u\theta_{\mathrm{res}}}\langle u_z^2\rangle^{1/2}\langle\theta_{\mathrm{res}}^2\rangle^{1/2}$, where $C_{u\theta_{\mathrm{res}}} = \langle u_z\theta_{\mathrm{res}}\rangle/[\langle u_z^2\rangle^{1/2}\langle\theta_{\mathrm{res}}^2\rangle^{1/2}]$ is the normalized correlation function. In Table II we list the Ra dependence for the above quantities that provide the appropriate corrections to the Nusselt number from Kraichnan's predictions [38] for the ultimate regime ($\mathrm{Nu} \sim \mathrm{Ra}^{1/2}$) to the experimentally observed $\mathrm{Nu} \sim \mathrm{Ra}^{0.30}$.

It is tempting to connect our findings to the ultimate regime of turbulent convection [20,21]. We conjecture that in the ultimate regime $C_{u\theta_{\mathrm{res}}}$ and θ_{res} as well as the coefficients c_i, would become independent of the Ra due to boundary layer detachment and hence yield $\mathrm{Nu} \sim \mathrm{Ra}^{1/2}$. We need input from experiments and numerical simulations to probe the above conjectures.

The exact relations of Shraiman and Siggia [39] yield

$$\epsilon_u = \frac{U^3}{d}\frac{(\mathrm{Nu} - 1)\mathrm{Ra}\,\mathrm{Pr}}{\mathrm{Pe}^3}. \qquad (7)$$

In the turbulent regime, $\mathrm{Nu} \sim \mathrm{Ra}^{0.32}$ and $\mathrm{Pe} \sim \mathrm{Ra}^{0.51}$, hence, $\epsilon_u \neq U^3/d$, rather than $\epsilon_u \sim (U^3/d)\mathrm{Ra}^{-0.21}$ is due the confinement of turbulence by the walls. In the viscous
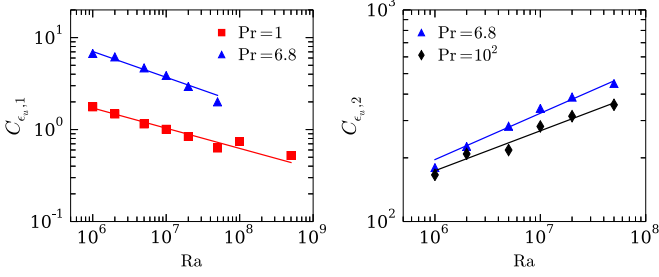
FIG. 6. The plots of normalized viscous dissipation rates $C_{\epsilon_u,1}$ (in the turbulent regime) and $C_{\epsilon_u,2}$ (in the viscous regime). $C_{\epsilon_u,1} \sim$ $\mathrm{Ra}^{-0.22}$ and $\mathrm{Ra}^{-0.25}$ for $\mathrm{Pr} = 1$ and 6.8, respectively, whereas $C_{\epsilon_u,2} \sim$ $\mathrm{Ra}^{0.22}$ and $\mathrm{Ra}^{0.19}$ for $\mathrm{Pr} = 6.8$ and 10^2, respectively. These results are in qualitative agreement with model predictions (see Table II).

regime,

$$\epsilon_u = \frac{\nu U^2}{d^2} \frac{(\mathrm{Nu} - 1)\mathrm{Ra}}{\mathrm{Pe}^2}. \tag{8}$$

Since $\mathrm{Nu} \sim \mathrm{Ra}^{0.33}$ and $\mathrm{Pe} \sim \mathrm{Ra}^{0.58}$ [24,29], we observe that $\epsilon_u \sim (\nu U^2/d^2)\mathrm{Ra}^{0.17}$. Note that, in a typical viscous scenario, $\epsilon_u \sim \nu U^2/d^2$. Hence the Ra dependence of c_4 and the correction of the viscous term from $\nu U/d^2$ are related to the boundary layers.

To quantify the scaling of the viscous dissipation rates given by Eqs. (7) and (8), we define two normalized viscous dissipation rates as

$$C_{\epsilon_u,1} = \frac{\epsilon_u}{U^3/d} = \frac{(\mathrm{Nu} - 1)\mathrm{Ra}\,\mathrm{Pr}}{\mathrm{Pe}^3} \sim \mathrm{Ra}^{-0.21}\mathrm{Pr}, \tag{9}$$

$$C_{\epsilon_u,2} = \frac{\epsilon_u}{\nu U^2/d^2} = \frac{(\mathrm{Nu} - 1)\mathrm{Ra}}{\mathrm{Pe}^2} \sim \mathrm{Ra}^{0.17}. \tag{10}$$

The correlation functions $C_{\epsilon_u,1}, C_{\epsilon_u,2}$ are suitable for the turbulent and viscous regimes, respectively. We compute these quantities using the numerical data obtained from numerical simulations and plot them as a function of the Ra in Fig. 6 and demonstrate that $C_{\epsilon_u,1} \sim \mathrm{Ra}^{-0.21}$ and $C_{\epsilon_u,2} \sim \mathrm{Ra}^{0.17}$. Our results demonstrate that the dissipation rates in RBC differ from those in unbounded flows due to the walls.

Let us estimate the ratio of the total dissipation rates (product of the dissipation rate and the appropriate volume) in the boundary layer ($D_{u,\mathrm{BL}}$) and in the bulk ($D_{u,\mathrm{bulk}}$). In the turbulent regime,

$$\frac{D_{u,\mathrm{BL}}}{D_{u,\mathrm{bulk}}} \approx \frac{(\epsilon_{u,\mathrm{BL}})(2A\delta_u)}{(\epsilon_{u,\mathrm{bulk}})(Ad - 2A\delta_u)} \approx \left(\frac{2\nu U^2/\delta_u^2}{U^3/d}\right)\frac{\delta_u}{d}$$

$$\approx 2\frac{d/\delta_u}{\mathrm{Re}} \approx 2\,\mathrm{Re}^{-1/2}, \tag{11}$$

since $\delta_u/d \sim \mathrm{Re}^{-1/2}$ [40]. Here δ_u is the thickness of the viscous boundary layers at the top and bottom plates, and A is the cross sectional area of these plates. The factor 2 is included to account for the dissipation near both plates. Equation (11) indicates that $D_{u,\mathrm{BL}} \ll D_{u,\mathrm{bulk}}$ for large Re's. In the viscous regime, the boundary layer spans the whole region ($2\delta_u \approx d$), therefore $D_{u,\mathrm{BL}}$ dominates $D_{u,\mathrm{bulk}}$. Also, our formula [Eq. (5)] includes both the turbulent and the viscous regimes.

Earlier Grossmann and Lohse [10–12] estimated U and the Nusselt number by invoking the exact relations of Shraiman and Siggia [39] and using the fact that the total dissipation is a sum of those in the bulk and in the boundary layers ($D_{u,\mathrm{bulk}}$ and $D_{u,\mathrm{BL}}$, respectively). Our derivation is an alternative to that of GL with an attempt to highlight the anisotropic effects arising due to the boundary layers that yield $\epsilon_u \neq U^3/d$ and $\epsilon_T \neq U\Delta^2/d$. Note that our derivation does not use the exact relations of Shraiman and Siggia [39] $\epsilon_{u,\mathrm{bulk}} \sim U^3/d$ and $\epsilon_{T,\mathrm{bulk}} \sim U\Delta^2/d$, where $\epsilon_{u,\mathrm{bulk}}$ and $\epsilon_{T,\mathrm{bulk}}$ are the bulk viscous and thermal dissipation rates, respectively.

IV. CONCLUSIONS

The agreement among our model, earlier experiments, and numerical simulations is remarkable, considering that our prediction is based on cubical box, whereas the experiments and numerical simulations employ cubical and cylindrical geometries. This result indicates that the Péclet scaling is *weakly* dependent on the aspect ratio or geometry and it can be reasonably well described by the nonlinear equation [Eq. (2)] which is based on the scaling of the large-scale quantities. This is one of the important conclusions of our paper as well as that of Grossmann and Lohse [10–12]. Note however that the discrepancies between the model predictions and the experimental results (see Fig. 5) could be due to the weak dependence of the Péclet number on geometry or aspect ratio.

The above observations indicate that the flow behavior in RBC differs significantly from the unbounded hydrodynamic turbulence for which we employ homogeneous and isotropic formalisms. Interestingly, in turbulent RBC, the buoyancy term is *nearly* canceled by the viscous term. This feature of RBC could be the reason for Kolmogorov's spectrum in RBC as reported by Kumar *et al.* [41]. The aforementioned wall effects should also be present in other bounded flows, such as in channels, pipes, rotating convection, spheres, and cylinders. The procedure adopted in this paper would yield similar formulas for the large-scale velocity and the dissipation rate for these systems.

To summarize, we derive a general formula for the large-scale velocity U or the Péclet number for RBC that is applicable for any Ra or Pr. Our formula provides reasonable fits to the results of earlier experiments and numerical simulations. We also compute the correlation function between u_z and θ that causes deviations of the Nusselt number from the theoretical prediction of $\mathrm{Nu} \sim \mathrm{Ra}^{1/2}$ to the experimentally observed $\mathrm{Nu} \sim \mathrm{Ra}^{0.30}$. In Table II, we also show how the dissipation rate ϵ_u and the temperature fluctuations in RBC get corrections from the usual formulas due to the boundary walls.

Our formulas discussed in this paper provide insight into the flow dynamics of RBC. These results will be useful in modeling convective flows in the interiors and atmospheres of stars and planets as well as in engineering applications.

APPENDIX: TEMPERATURE PROFILE AND BOUNDARY LAYER

The temperature is a function of x, y, and z, i.e., $T(x,y,z)$. However, as shown in Fig. 1, its planar average $T_m(z)$ is approximately $1/2$ in the bulk, and it varies rapidly in the boundary layers. We can approximate $T_m(z)$ as

$$T_m(z) = \begin{cases} 1 - \frac{z}{2\delta_T} & \text{for } 0 < z < \delta_T, \\ 1/2 & \text{for } \delta_T < z < 1 - \delta_T, \\ \frac{1-z}{2\delta_T} & \text{for } 1 - \delta_T < z < 1, \end{cases} \quad (A1)$$

where δ_T is the thickness of the thermal boundary layers at the top and bottom plates. In RBC, it is customary to describe the flow using the temperature fluctuation from the conduction state θ defined as

$$T(x,y,z) = \theta(x,y,z) + 1 - z. \quad (A2)$$

For the above, we have normalized the temperature fluctuation using the temperature difference between the plates and the vertical coordinate using the vertical distance between the plates. When we perform averaging of Eq. (A2) over the xy planes, we obtain

$$\theta_m(z) = T_m(z) + z - 1, \quad (A3)$$

where $\theta_m(z)$ is

$$\theta_m(z) = \begin{cases} z\left(1 - \frac{1}{2\delta_T}\right) & \text{for } 0 < z < \delta_T, \\ z - 1/2 & \text{for } \delta_T < z < 1 - \delta_T, \\ (z-1)\left(1 - \frac{1}{2\delta_T}\right) & \text{for } 1 - \delta_T < z < 1, \end{cases} \quad (A4)$$

which is exhibited in Fig. 1. For a pair of thin boundary layers, the Fourier transform of $\theta_m(z)$, $\hat{\theta}_m(k_z)$ is dominated by the contributions from the bulk, that is,

$$\hat{\theta}_m(k_z) = \int_0^1 \theta_m(z) \sin(k_z \pi z) dz \approx \int_0^1 (z - 1/2) \sin(k_z \pi z) dz$$

$$\approx \begin{cases} -\frac{1}{\pi k_z} & \text{for even } k_z, \\ 0, & \text{otherwise.} \end{cases} \quad (A5)$$

It is interesting to note that the corresponding velocity mode $\hat{u}_z(0,0,k_z) = 0$ because of the incompressibility condition $\mathbf{k} \cdot \hat{\mathbf{u}}(0,0,k_z) = k_z \hat{u}_z(0,0,k_z) = 0$. Also, $\hat{u}_{x,y}(0,0,k_z) = 0$ when we assume an absence of a mean horizontal flow on any horizontal plane. Hence, the momentum equation for the Fourier mode $(0,0,k_z)$ is

$$-ik_z \hat{\sigma}_m(0,0,k_z) + \alpha g \hat{\theta}_m(0,0,k_z) = 0, \quad (A6)$$

and it does not involve the velocity field. In the real space, the above equation translates to $d\sigma_m/dz = \alpha g \theta_m(z)$. For the Fourier modes other than $(0,0,k_z)$, the momentum equation is

$$\frac{\partial \hat{\mathbf{u}}(\mathbf{k})}{\partial t} = -i \sum_{\mathbf{p}+\mathbf{q}=\mathbf{k}} [\mathbf{k} \cdot \hat{\mathbf{u}}(\mathbf{q})] \hat{\mathbf{u}}(\mathbf{p}) - i\mathbf{k}\hat{\sigma}_{\text{res}}(\mathbf{k})$$

$$+ \alpha g \hat{\theta}_{\text{res}}(\mathbf{k})\hat{z} - \nu k^2 \hat{\mathbf{u}}(\mathbf{k}). \quad (A7)$$

We denote the participating temperature field in the above equation as residual temperature θ_{res} and the residual pressure field as σ_{res}, and they are defined as

$$\theta_{\text{res}} = \theta - \theta_m, \quad (A8)$$

$$\sigma_{\text{res}} = \sigma - \sigma_m. \quad (A9)$$

Thus, the large-scale velocity U depends on θ_{res} and σ_{res}.

[1] S. B. Pope, *Turbulent Flows* (Cambridge University Press, Cambridge, U.K., 2000).

[2] P. A. Davidson, *Turbulence: An Introduction for Scientists and Engineers* (Oxford University Press, Oxford, 2004).

[3] M. Lesieur, *Turbulence in Fluids—Stochastic and Numerical Modelling* (Kluwer Academic, Dordrecht, 2008).

[4] U. Frisch, *Turbulence: The Legacy of A. N. Kolmogorov* (Cambridge University Press, Cambridge, U.K., 2011).

[5] P. A. Davidson, *Turbulence in Rotating Stratified and Electrically Conducting Fluids* (Cambridge University Press, Cambridge, U.K., 2013).

[6] G. Ahlers, S. Grossmann, and D. Lohse, Rev. Mod. Phys. **81**, 503 (2009).

[7] E. D. Siggia, Annu. Rev. Fluid Mech. **26**, 137 (1994).

[8] D. Lohse and K. Q. Xia, Annu. Rev. Fluid Mech. **42**, 335 (2010).

[9] F. Chillà and J. Schumacher, Eur. Phys. J. E **35**, 58 (2012).

[10] S. Grossmann and D. Lohse, J. Fluid Mech. **407**, 27 (2000).

[11] S. Grossmann and D. Lohse, Phys. Rev. Lett. **86**, 3316 (2001).

[12] S. Grossmann and D. Lohse, Phys. Rev. E **66**, 016305 (2002).

[13] R. Stevens, E. P. Poel, S. Grossmann, and D. Lohse, J. Fluid Mech. **730**, 295 (2013).

[14] Y. B. Xin and K. Q. Xia, Phys. Rev. E **56**, 3010 (1997).

[15] S. Cioni, S. Ciliberto, and J. Sommeria, J. Fluid Mech. **335**, 111 (1997).

[16] X. L. Qiu and P. Tong, Phys. Rev. Lett. **87**, 094501 (2001).

[17] G. Ahlers and X. Xu, Phys. Rev. Lett. **86**, 3320 (2001).

[18] J. J. Niemela, L. Skrbek, K. R. Sreenivasan, and R. J. Donnelly, J. Fluid Mech. **449**, 169 (2001).

[19] S. Lam, X.-D. Shang, S.-Q. Zhou, and K.-Q. Xia, Phys. Rev. E **65**, 066306 (2002).

[20] P. Urban, P. Hanzelka, T. Kralik, V. Musilova, A. Srnka, and L. Skrbek, Phys. Rev. Lett. **109**, 154301 (2012).

[21] X. He, D. Funfschilling, H. Nobach, E. Bodenschatz, and G. Ahlers, Phys. Rev. Lett. **108**, 024502 (2012).

[22] R. Camussi and R. Verzicco, Phys. Fluids **10**, 516 (1998).

[23] M. van Reeuwijk, H. J. J. Jonker, and K. Hanjalić, Phys. Rev. E **77**, 036311 (2008).

[24] G. Silano, K. R. Sreenivasan, and R. Verzicco, J. Fluid Mech. **662**, 409 (2010).

[25] J. Bailon-Cuba, M. S. Emran, and J. Schumacher, J. Fluid Mech. **655**, 152 (2010).

[26] J. D. Scheel, E. Kim, and K. R. White, J. Fluid Mech. **711**, 281 (2012).

[27] M. K. Verma, P. K. Mishra, A. Pandey, and S. Paul, Phys. Rev. E **85**, 016310 (2012).

[28] S. Wagner and O. Shishkina, Phys. Fluids **25**, 085110 (2013).

[29] A. Pandey, M. K. Verma, and P. K. Mishra, Phys. Rev. E **89**, 023006 (2014).

[30] S. Horn, O. Shishkina, and C. Wagner, J. Fluid Mech. **724**, 175 (2013).

[31] OPENFOAM, Openfoam: The Open Source cfd Toolbox (2015), http://www.openfoam.org.

[32] G. Grötzbach, J. Comput. Phys. **49**, 241 (1983).

[33] O. Shishkina, R. Stevens, S. Grossmann, and D. Lohse, New J. Phys. **12**, 075022 (2010).

[34] J. D. Scheel and J. Schumacher, J. Fluid Mech. **758**, 344 (2014).

[35] G. Schubert, D. L. Turcotte, and P. Olson, *Mantle Convection in the Earth and Planets* (Cambridge University Press, Cambridge, U.K., 2001).

[36] D. L. Turcotte and G. Schubert, *Geodynamics* (Cambridge University Press, Cambridge, U.K., 2002).

[37] A. Galsa, M. Herein, L. Lenkey, M. P. Farkas, and G. Taller, Solid Earth **6**, 93 (2015).

[38] R. H. Kraichnan, Phys. Fluids **5**, 1374 (1962).

[39] B. I. Shraiman and E. D. Siggia, Phys. Rev. A **42**, 3650 (1990).

[40] L. D. Landau and E. M. Lifshitz, *Fluid Mechanics* (Pergamon, Oxford, 1987).

[41] A. Kumar, A. G. Chatterjee, and M. K. Verma, Phys. Rev. E **90**, 023016 (2014).